

# Magnetic Phase Diagram of YbRh<sub>2</sub>Si<sub>2</sub>: the Influence of Hyperfine Interactions

J. Knapp, L. V. Levitin, J. Nyéki, B. Cowan, and J. Saunders  
*Department of Physics, Royal Holloway University of London, TW20 0EX, Egham, UK. \**

M. Brando and C. Geibel  
*Max Planck Institute for Chemical Physics of Solids,  
Nöthnitzer Straße 40, 01187 Dresden, Germany.*

K. Kliemt and C. Krellner  
*Physikalisches Institut, Max-von-Laue-Straße 1, 60438 Frankfurt am Main, Germany.*  
(Dated: January 30, 2025)

We report the determination of the magnetic phase diagram of the heavy fermion metal YbRh<sub>2</sub>Si<sub>2</sub> in magnetic fields up to 70 mT applied perpendicular to the crystallographic *c*-axis. By a combination of heat capacity, magneto-caloric, and magneto-resistance measurements we map two antiferromagnetic phases: the electronic AFM1 below 70 mK and electro-nuclear AFM2 below 1.5 mK. The measurements extend into the microkelvin regime to explore the quantum phase transitions in this system. We demonstrate how the hyperfine interaction significantly modifies the phase diagram and the putative field-tuned quantum critical point. The determination of the rich magnetic properties of YbRh<sub>2</sub>Si<sub>2</sub> is essential to understanding the interplay of the two magnetic orders and superconductivity in this compound.

The heavy fermion metal YbRh<sub>2</sub>Si<sub>2</sub> has been extensively studied for many years as an example of a system that can be tuned towards quantum criticality, by chemical pressure or by magnetic field [1–7]. Often, superconductivity emerges in heavy fermion metals when they are tuned to the quantum critical point (QCP); the effect of pressure on multiple Ce-based compounds being well established [8]. Following the first Yb-based superconducting heavy fermion  $\beta$ -YbAlB<sub>4</sub> [9], more recently the discovery of superconductivity in YbRh<sub>2</sub>Si<sub>2</sub> [10–12] makes it only the second example of an Yb-based superconductor. The interplay of magnetism and superconductivity is a central question in the study of strongly correlated electronic systems. In a material where superconductivity emerges out of magnetically ordered states, like YbRh<sub>2</sub>Si<sub>2</sub>, it is clear that a general requirement is the complete determination of the magnetic phase diagram. This is the subject of this Letter.

We report a combination of calorimetry and electrical transport studies with magnetic field applied in the *ab*-plane of tetragonal single crystals of YbRh<sub>2</sub>Si<sub>2</sub>, thereby determining the magnetic phase diagram shown in Fig. 1. It features two antiferromagnetic phases, AFM1 [1] and AFM2 [13], terminating at two field-tuned quantum phase transitions, that we precisely determine. Measurements at ultra-low temperatures, below 1 mK, were essential for this study, requiring novel experimental techniques [12, 14]. The stability of AFM2 and the backturn of the critical field of AFM1 are both manifestations of the hyperfine interaction of Yb.

YbRh<sub>2</sub>Si<sub>2</sub> features strong anisotropy of the Fermi surface [7, 15–19] and electronic magnetism [1]. The AFM1 phase, suppressed by in-plane field of 57 mT or an order

of magnitude larger field along the *c*-axis [1], features only very small ordered moments,  $\mu_e \approx 0.002 \mu_B$  [20], developing out of partially Kondo-screened Yb local moments  $1.4 \mu_B$  [1], where  $\mu_B$  is the Bohr magneton. Ordering of the small moments along the magnetically-hard *c*-axis

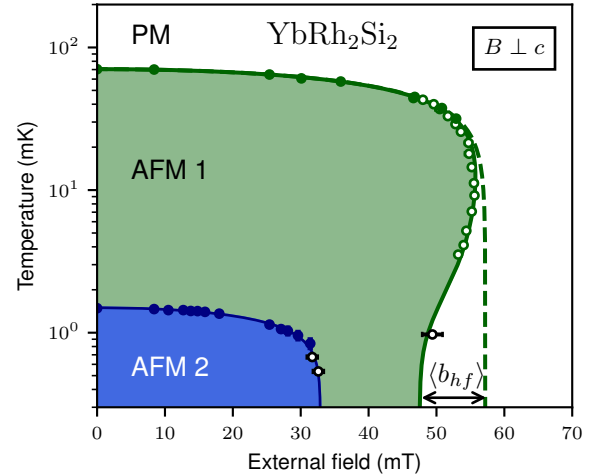


FIG. 1. Phase diagram of the two antiferromagnetic orders in YbRh<sub>2</sub>Si<sub>2</sub>. The critical field  $B_N(T)$  of the AFM1 phase (solid green line) shows a non-monotonic temperature dependence. We understand this  $T \rightarrow 0$  backturn from the asymptote  $B_N^*$  (dashed green line) as an effect of the hyperfine field  $\langle b_{hf} \rangle$ , which adds to the external field according to Eq. (1). The critical field  $B_A(T)$  of the electro-nuclear AFM2 phase shows a regular behavior. The heat capacity peaks are shown by filled circles, magneto-caloric sweep signature by open black circles, and magneto-resistance by open green circles. Calorimetry and transport studies were done on two different samples.

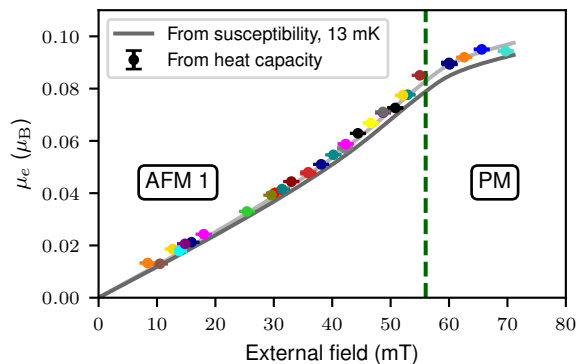


FIG. 2. Growth of the polarised electronic magnetic moment  $\mu_e$  with in-plane magnetic field at 13 mK, calculated as the integral of magnetic susceptibility [33], and determined from the heat capacity using the *Hyperfine Schottky model* (see SM). Scaling the susceptibility data by a factor of 1.05 (light grey) removes a small systematic discrepancy between the two methods.

has been proposed [21], but the nature of this order is not understood, and neither is the putative quantum criticality proposed for the suppression of this order with magnetic field. Current theories include the *local quantum criticality* [22–25], see also [4, 5, 26–28], and theories invoking strong coupling of fermions and spin fluctuations into critical quasiparticles [29–32]. Until recently, the magnetic phase diagram of AFM1 had only been studied down to 20 mK, leaving the fate of this putative QCP unresolved. Here we show that the large hyperfine interaction of Yb plays a key role.

A remarkable property of AFM1 is the strong paramagnetic response to in-plane field. The evolution of the 4f electronic moment  $\mu_e$  of Yb with external field can be inferred directly from the measurements of magnetic susceptibility  $\chi$  at 13 mK [33]. The result is shown in Fig. 2 in terms of the moment per Yb ion. This measurement corresponds to a single Yb ion susceptibility  $\chi_{\text{ion}} \equiv \mu_e/B_{\text{ext}} = \chi_m/\mu_0 N_A \approx 1.2 \mu_B/\text{T}$  (at 13 mK and zero field), where  $\chi_m$  is the molar susceptibility [33]. This is equivalent to a dimensionless susceptibility  $\chi = 0.18$ . The shape of the  $\mu_e(B_{\text{ext}})$  curve reflects a maximum in susceptibility at about 50 mT [33]. Fig. 2 also shows the excellent agreement with  $\mu_e(B_{\text{ext}})$  inferred from the nuclear heat capacity, as discussed in detail later in this Letter. The established  $\mu_e(B_{\text{ext}})$  is the key input for our analysis of the influence of the hyperfine interaction on the AFM1/PM phase boundary.

Recently we identified a new phase, here denoted AFM2, as an electro-nuclear spin density wave, the transition to which occurs as a direct result of the hyperfine interaction [13]. The staggered magnetic moments were found to lie in the ab-plane and to be continuously suppressed from  $\mu_e \sim 0.1 \mu_B$  to zero by in-plane magnetic field. Ref. [13] also introduces the use of the heat capac-

ity of nuclear spins as a probe of the electronic moments hyperfine-coupled to them, a method we develop further here.

Our primary experimental technique is calorimetry [14], modified from Ref. [13] to allow adiabatic measurements to higher fields. The heat capacity peaks at  $T_A$  (onset of AFM2) and  $T_N$  (onset of AFM1), Fig. 3, give extremely sharp signatures of the transitions in low external field  $B_{\text{ext}}$ . They clearly demonstrate zero slope  $\partial T_{A/N}/\partial B_{\text{ext}}$  at  $B_{\text{ext}} \rightarrow 0$  for both phase boundaries. This is in contrast to the finite  $\partial T_A/\partial B_{\text{ext}}$  derived from magnetic susceptibility measurements [10]; we note that those studies would have been affected by the diamagnetic screening associated with superconductivity.

When  $\partial T_{A/N}/\partial B_{\text{ext}}$  is high, we must use field sweep methods to identify the phase transitions: the magneto-caloric sweeps, Fig. 4, and magneto-resistance, Fig. 5. The magneto-caloric field sweeps allow us to pin-point

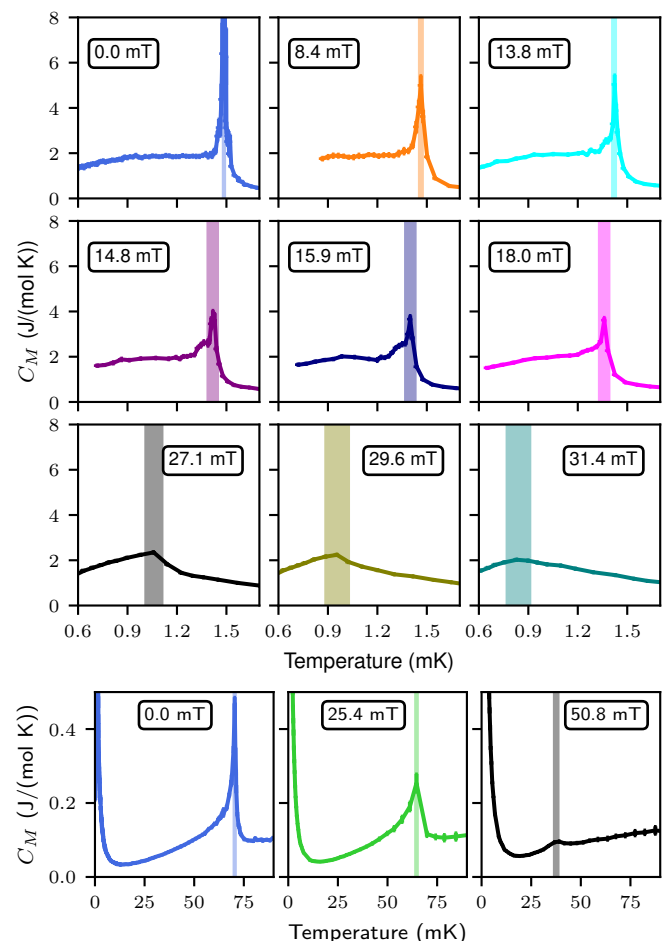


FIG. 3. Evolution of the  $T_A$  (top) and  $T_N$  (bottom) transition peaks with magnetic field. Estimated transition temperature and its uncertainty are marked by vertical bands. Weak effects of measurement preparation conditions on the position and shape of the AFM2 transition signature are discussed in the SM.

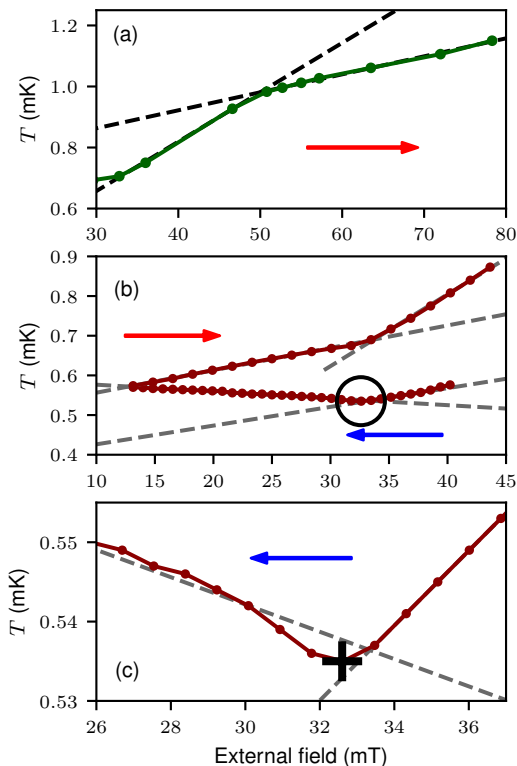


FIG. 4. Examples of adiabatic magneto-caloric sweeps with linear fits above and below the transition. Direction of the field change indicated by the arrows. (a) magnetization sweep from AFM1 to PM; (b) (de-)magnetization sweeps across the AFM1/2 boundary; (c) detail of the de-magnetization sweep in (b) highlighted by the circle. A small dip is observed at the AFM1/AFM2 phase transition (in both directions) and here marked by the cross. These features are used as transition points in Fig. 1.

the AFM1/PM and AFM2/AFM1 transitions at a temperature below 1 mK, thus close to the quantum phase transition end-points. The method again uses the nuclear spin system as the witness of the electronic magnetism. Clear features are observed in the response of temperature to varying the field, thanks to the excellent adiabatic isolation of our calorimeter [14]. Crossing the critical field of AFM1, see Fig. 4a, the change of slope of the adiabatic magneto-caloric sweeps is directly linked to the kink in the field dependence of magnetic susceptibility (the “ $B_2$ ” feature in Ref. [33]). The AFM1/AFM2 phase transition is also marked by a change of slope, see Fig. 4b,c. The weaker magneto-caloric effect in the AFM2 phase is a consequence of staggered nuclear polarization of the spin-density wave, that considerably bounds the nuclear entropy.

The AFM1/PM boundary is also determined between 4 and 45 mK from magneto-resistance measurements, Fig. 5, exploiting our SQUID-based measurements of the complex sample impedance  $Z$  with 10 n $\Omega$  resolution [12]. We identify a minimum in  $\partial \text{Re} Z / \partial B_{\text{ext}}$  as the signature

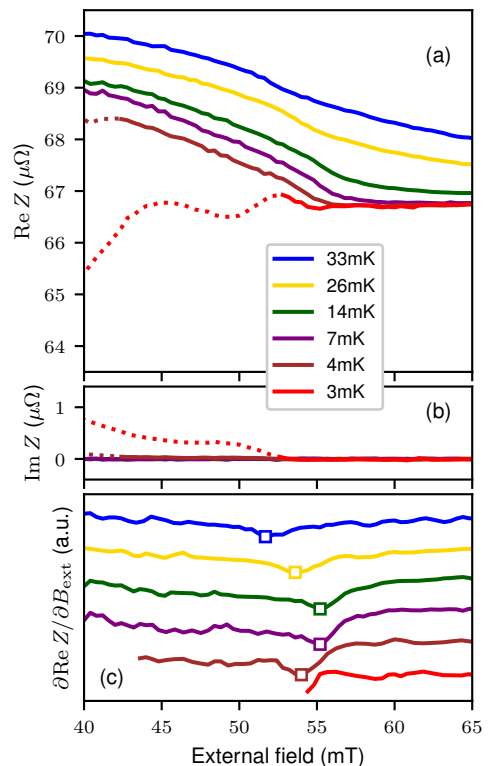


FIG. 5. Measurements of magneto-resistance (a) identify the AFM1/PM phase boundary by a minimum in  $\partial \text{Re} Z / \partial B_{\text{ext}}$  (c). (b) At the lowest temperature, this procedure is interrupted by the onset of superconductivity, revealed by the appearance of  $\text{Im} Z$  associated with kinetic inductance [12]. On these grounds the data where  $\text{Im} Z > 0.05 \mu\Omega$  (shown with dotted lines) were excluded from the analysis.

of the phase transition. This is justified by the coincidence of this magneto-resistance signature with the heat capacity peaks above 32 mK, see Fig. 1. The magneto-resistance method requires the sample to be in the normal state, and it is interrupted at 3 mK by the onset of superconductivity, see Fig. 5.

The above combination of measurement methods has enabled us to probe the PM/AFM1/AFM2 phase diagram into the  $\mu\text{K}$  regime. The AFM2 dome,  $B_A(T)$ , Fig. 1, is well described by a cubic polynomial fit to  $B_A^2(T)$  (See Eq. (S12) in SM). This, and the temperature/magnetic field range of the measurements, allows us to determine a critical field in the  $T = 0$  limit of 33 mT, close to our original prediction of 36 mT [13].

The AFM1/PM phase boundary above 20 mK can also be described by a phenomenological ansatz for  $B_N^2(T)$  of the same form. However, at lower temperatures we observe a clear “backturn”, i.e. decrease of the critical field as temperature is lowered. We will show that the backturn is fully accounted for by the hyperfine interaction, with the relevant hyperfine field saturating at around 10 mT at the lowest temperatures. Consequently, the external critical field  $B_N$  at  $T = 0$  is

47 mT, rather than 57 mT conventionally extrapolated from high-temperature measurements [1].

We now explain in more detail the procedure to calculate the AFM1/PM phase boundary, in terms of known system properties, which as can be seen from Fig. 1 is in full agreement with observations. The dominant hyperfine interaction in  $\text{YbRh}_2\text{Si}_2$  involves the 4f electron orbitals of Yb [7, 34–37] and arises in the Yb isotopes with non-zero nuclear spin:  $^{171}\text{Yb}$  ( $I = 1/2$ ) and  $^{173}\text{Yb}$  ( $I = 5/2$ ) with natural abundances 0.14 and 0.16 respectively. The hyperfine constant of Yb is particularly strong,  $A_{\text{hf}} = 102 \pm 3 \text{ T}/\mu_{\text{B}}$  [38–41]. In  $\text{YbRh}_2\text{Si}_2$  it combines with the particular strong dependence of 4f moment on in-plane field  $\mu_e(B_{\text{ext}})$  with dramatic effects. The hyperfine interaction can be expressed as follows:  $U_{\text{hf}} = A_{\text{hf}} \boldsymbol{\mu}_e \cdot \boldsymbol{\mu}_n = -\mathbf{B}_{\text{hf}} \cdot \boldsymbol{\mu}_n = -\mathbf{b}_{\text{hf}} \cdot \boldsymbol{\mu}_e$ . Here  $\mathbf{B}_{\text{hf}} = -A_{\text{hf}} \boldsymbol{\mu}_e$  is the hyperfine field exerted by the magnetic moment  $\boldsymbol{\mu}_e$  of the electron on the nuclear magnetic moment  $\boldsymbol{\mu}_n$ ; the reciprocal field  $\mathbf{b}_{\text{hf}} = -A_{\text{hf}} \boldsymbol{\mu}_n$  is felt by the electron.  $B_{\text{hf}}$  dominates the nuclear energy level splitting ( $B_{\text{hf}} \gg B_{\text{ext}}$ ) for  $^{171}\text{Yb}$  ( $I = 1/2$ ), while in the case of  $^{173}\text{Yb}$  ( $I = 5/2$ ) the known quadrupolar interaction (See Eq. (S3) in SM) must also be taken into account. The temperature-dependent nuclear polarization is determined self-consistently with  $\mu_e(B_{\text{ext}})$ , taking into account  $b_{\text{hf}}$ . We note that inside AFM1, the staggered magnetization is insignificant and the hyperfine fields are essentially collinear with the external field.

Figure 6 shows an estimate of  $b_{\text{hf}}(T)$  for both isotopes at the critical field of AFM1, using the electronic moment  $\mu_e = 0.085 \mu_{\text{B}}$  measured at this phase boundary at 13 mK, see Fig. 2. We find that the backturn is compensated if we add the average  $\langle b_{\text{hf}} \rangle$  over the Yb isotopes to  $B_N$ . Thus we propose that the growth of paramagnetic moments  $\mu_e$  and the suppression of AFM1 order is driven by the *effective field*

$$B^* = B_{\text{ext}} + \langle b_{\text{hf}} \rangle. \quad (1)$$

In terms of this effective field the AFM1/PM phase boundary  $B_N^*(T) = B_N(T) + \langle b_{\text{hf}}(T, \mu_e(B_N^*(T))) \rangle$  is well described by a cubic polynomial fit to  $B_N^*(T)$  over the full temperature range (See Eq. (S11) in SM). In the temperature-effective field plane this phase boundary approaches the quantum phase transition vertically, with no backturn, see Fig. S1 in SM.

The field dependence of electronic moments  $\mu_e(B_{\text{ext}})$  at 13 mK, shown in Fig. 2, is inferred from the heat capacity measured between 1.7 and 13 mK, taking into account the gradual increase  $\mu_e$  on further cooling in a fixed external field driven by  $\langle b_{\text{hf}}(T) \rangle$ . This improved *hyperfine Schottky model* resolves the discrepancy between the data and the Schottky model with temperature-independent  $\mu_e(B_{\text{ext}})$  observed in Ref. [13]. We emphasize that  $\mu_e$  obtained from this method is in good agreement with the integral of the magnetic susceptibility [33], also plotted in Fig. 2. From these data we derive  $\mu_e(B^*)$ , assuming

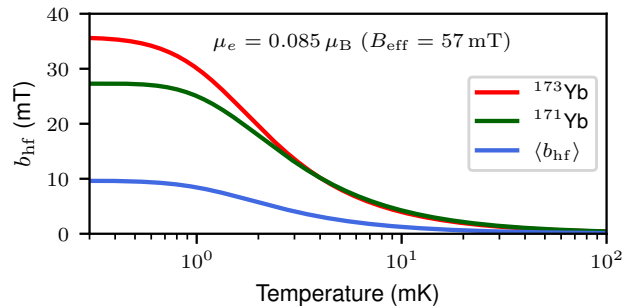


FIG. 6. Hyperfine fields on the  $^{171}\text{Yb}$  and  $^{173}\text{Yb}$  sites and the spatial average  $\langle b_{\text{hf}} \rangle$  over all Yb isotopes as a function of temperature for a constant electronic moment  $\mu_e = 0.085 \mu_{\text{B}}$ . This value of  $\mu_e$  corresponds to  $B^* = 57 \text{ mT}$ , the critical effective field of AFM1 below 13 mK. The quadrupolar splitting of  $^{173}\text{Yb}$  in the crystalline electric field is taken into account [13]. Details in SM.

it to be temperature independent, and self-consistently calculate  $b_{\text{hf}}(B_{\text{ext}}, T)$ , feeding into the determination of  $B_N^*(T)$  from the measured phase transition signatures (details in SM) [42].

Although the local hyperfine field  $b_{\text{hf}}$  is not uniform because of the Yb isotopic composition and short-ranged nature of the hyperfine interaction, the fact that its effect is accounted for by the average over Yb sites  $\langle b_{\text{hf}} \rangle$  is, we believe, a powerful insight into the nature of the heavy fermion state. A full microscopic theory of this finding is desirable.

A detailed study with  $B_{\text{ext}} \parallel c$ , requiring field-swept measurements in a new higher-field set-up, is beyond the scope of this work. A preliminary phase diagram for this field orientation is significantly different from  $B_{\text{ext}} \perp c$ , with evidence for a PM/AFM1/AFM2 poly-critical point [12], resembling  $\text{Yb}(\text{Rh}_{0.82}\text{Co}_{0.18})_2\text{Si}_2$  [21]. The relationship between the magnetic structure of the electro-nuclear order of the AFM2 phase in  $\text{YbRh}_2\text{Si}_2$  and the eponymous phase in Ref. [21] remains an open question.

Our results strongly motivate future experiments on isotopically enriched samples using the techniques we have developed. In the absence of active nuclear spins, for example in  $^{174}\text{YbRh}_2\text{Si}_2$  [7], we predict the external critical field of the AFM1 phase to coincide with the  $B_N^*(T)$  line and the AFM2 phase to be absent. On the other hand, we estimate enhanced backturn in  $^{171}\text{YbRh}_2\text{Si}_2$  and  $^{173}\text{YbRh}_2\text{Si}_2$ , where the hyperfine fields saturate in the  $T \rightarrow 0$  limit at 27 mT and 35 mT respectively, see Fig. 6. Mean field theory [13] predicts an enhancement in  $T_A$  by a factor of 3 in zero magnetic field. Moreover, in these materials the nuclear spins form a regular lattice, in contrast to natural  $\text{YbRh}_2\text{Si}_2$ , which may have unexpected consequences on the AFM2 phase.

The theoretical framework for treating the impact of hyperfine interactions on quantum criticality has re-

cently been reported [43]. Hyperfine effects have been experimentally investigated in the transverse-field Ising ferromagnet LiHoF<sub>4</sub> [44, 45], where findings include a shift in quantum critical field and softening of collective electro-nuclear modes near the QCP. In the compound YbCu<sub>4.6</sub>Au<sub>0.4</sub> it was hypothesized that the quantum critical fluctuations do not originate from purely electronic states but from entangled electro-nuclear states, due to the low Kondo and RKKY energy scales [46]. Diverse influences of hyperfine interactions on superconductivity and antiferroquadrupolar order have been found in PrOs<sub>4</sub>Sb<sub>12</sub> [47].

In conclusion, we report diverse hyperfine effects in YbRh<sub>2</sub>Si<sub>2</sub>, which has been referred to as a “canonical heavy fermion” material [10]. YbRh<sub>2</sub>Si<sub>2</sub> is a unique

laboratory of heavy fermion physics, featuring interplay between magnetism and superconductivity, and cooperative electro-nuclear phenomena. This letter reports two quantum phase transitions. Future theoretical and experimental work should investigate the potential novel quantum criticality that may emerge as a result of the hyperfine interaction [43], and the effect of isotopic composition of Yb on the phase diagram.

This work was supported by the European Microkelvin Platform, by the European Union’s Horizon 2020 Research and Innovation programme under grant agreement no. 824109. It was also supported by the Deutsche Forschungsgemeinschaft (DFG, German Research Foundation) through grants Nos. BR 4110/1-1, KR3831/4-1, and via the TRR 288, (422213477, project A03).

## Supplemental Material

### CALCULATION OF HYPERFINE FIELDS

At the center of the modeling procedures discussed in the following sections is the hyperfine interaction. We choose the coordinate system with  $x$  axis aligned with the direction of the in-plane magnetic field and  $z$  axis pointing along the  $c$  axis. Then, restricting our considerations to the AFM1 and PM phases and ignoring the small staggered magnetization of AFM1, all relevant vectors are aligned with the  $x$  axis. For a given temperature  $T$  and field of the reverse action  $B_{\text{hf}} = -A_{\text{hf}}\mu_e$  we calculate the  $x$  components of the hyperfine fields

$$b_{\text{hf}}^{171/173} = -A_{\text{hf}}\mu_n = -A_{\text{hf}}g\mu_N I_x, \quad (\text{S1})$$

where the static nuclear polarization

$$I_x = \sum_i p_i \langle \psi_i | \hat{I}_x | \psi_i \rangle, \quad (\text{S2})$$

is determined by the Boltzmann factors  $p_i = \exp(-E_i/k_B T) / \sum_i \exp(-E_i/k_B T)$  and eigenvectors  $\psi_i$  and eigenvalues  $E_i$  of the nuclear Hamiltonian

$$\hat{H} = -g\mu_N \hat{I}_x B_{\text{hf}} + \frac{e^2 q Q}{4I(2I-1)} (3\hat{I}_z^2 - I(I+1)). \quad (\text{S3})$$

For the quadrupolar parameters  $eq$  and  $Q$  and other details of this Hamiltonian, see main body and supplementary material of Ref. [13].

From thus determined hyperfine fields  $b_{\text{hf}}^{171}$  and  $b_{\text{hf}}^{173}$  and the natural abundances  $n_{171} = 0.14$  and  $n_{173} = 0.16$  of the magnetically active Yb isotopes we compute the average hyperfine field across all Yb sites

$$\langle b_{\text{hf}} \rangle = n_{171} b_{\text{hf}}^{171} + n_{173} b_{\text{hf}}^{173}.$$

### EFFECTIVE FIELD IN SPIN 1/2 MODEL

Here we consider the simple model with  $N$  Yb sites,  $N_n$  of which host nuclear spins 1/2, and the remaining nuclei are spinless [13, Eqs. (S15)-(S23)]. We restrict ourselves to AFM1 and PM phases, where there is no significant staggered magnetization, so  $\mu_e$  coincides with the paramagnetic moment (in Ref. [13] this is called  $\mu_P$ ). In the strongly-correlated electron system of YbRh<sub>2</sub>Si<sub>2</sub> we assume  $\mu_e$  to be the same on Yb sites with and without nuclear spins. Then the Gibbs free energy is

$$G(T, B_{\text{ext}}; \mu_e) = -N_n k_B T \log \left( 2 \cosh \frac{g\mu_N A_{\text{hf}} \mu_e}{2k_B T} \right) + N[\beta\mu_e^2 - B_{\text{ext}}\mu_e]. \quad (\text{S4})$$

For each site with a non-zero nuclear spin the thermal average of the nuclear polarization is

$$\langle I_x \rangle = -\frac{1}{2} \tanh \frac{g\mu_N A_{\text{hf}} \mu_e}{2k_B T}, \quad (\text{S5})$$

and after averaging over the Yb sites with and without nuclear spins we get the effective hyperfine field

$$\langle b_{\text{hf}} \rangle = \frac{N_n}{N} \frac{g\mu_N A_{\text{hf}}}{2} \tanh \frac{g\mu_N A_{\text{hf}} \mu_e}{2k_B T}. \quad (\text{S6})$$

The equilibrium  $\mu_e(T, B)$  is determined by minimising the free energy given by Eq. (S4),

$$\frac{\partial G}{\partial \mu_e} = -N_n \frac{g\mu_N A_{\text{hf}}}{2} \tanh \frac{g\mu_N A_{\text{hf}} \mu_e}{2k_B T} + 2N\beta\mu_e - NB_{\text{ext}} = 0. \quad (\text{S7})$$

This condition can be rewritten as

$$\frac{\partial G}{\partial \mu_e} = N(2\beta\mu_e - B_{\text{ext}} - \langle b_{\text{hf}} \rangle) = 0. \quad (\text{S8})$$

The solution of Eq. (S8) is

$$\mu_e = [B_{\text{ext}} + \langle b_{\text{hf}} \rangle] / 2\beta = B^* / 2\beta, \quad (\text{S9})$$

thus the paramagnetic moments  $\mu_e$  are driven by the effective field  $B^*$  in a temperature-independent way.

### EFFECTIVE MAGNETIZATION CURVE

Down to 13 mK we neglect the hyperfine field  $\langle b_{\text{hf}} \rangle$ , which is at most 1 mT, thus in this regime  $B^* \approx B_{\text{ext}}$ . At 13–40 mK the temperature dependence of the magnetic susceptibility  $\chi_m(B_{\text{ext}})$  of the AFM1 phase [33], and therefore of the magnetization curve  $\mu_e(B_{\text{ext}})$  is weak, consistent with temperature-independent  $\mu_e(B^*)$  derived in Eq. (S9). We assume  $\mu_e(B^*)$  to have this property, and derive this dependence from the 13 mK susceptibility measurements [33] as

$$\begin{aligned} \mu_e(B^*, T) &\approx \mu_e(B_{\text{ext}}, 13 \text{ mK}) \\ &= \int_{B=0}^{B_{\text{ext}}} \frac{1.05 \chi_m(B, 13 \text{ mK})}{\mu_0 N_A} dB \end{aligned} \quad (\text{S10})$$

We apply the 1.05 scaling factor to the  $\chi_m(B, T)$  data from Ref. [33], since this yields a good match with  $\mu_e(B^*)$  derived from heat capacity, see Fig. 2 of the main text and the next section.

### HYPERFINE SCHOTTKY MODEL

Fig. 2 in the main body shows a detailed study of the growth of the electronic moment with external magnetic field inside the AFM1 order and across the AFM1/PM boundary. Our previous discussion of this dependence in Ref. [13] (see Fig. 2 there), neglected the effect of the hyperfine field  $b_{\text{hf}}$ . Here we show how it can be taken into account in the analysis of the heat capacity measurements. The fitting at 1.7–13 mK of the high-temperature “tails” of the Schottky-like heat capacity peaks is illustrated in Fig. S1.

The *Hyperfine Schottky model* considers the exposure of the nuclear magnetic moments to the hyperfine field  $B_{\text{hf}}(T) = A_{\text{hf}} \mu_e(T)$ , where the value of the electronic moment  $\mu_e(T)$  in AFM1 increases as temperature is lowered from the high temperature value  $\mu_e^\infty \approx \mu_e(13 \text{ mK})$ . This is a result of the temperature-dependent hyperfine field  $\langle b_{\text{hf}} \rangle$  acting additionally on the electronic moment.

At a fixed  $B_{\text{ext}}$  we calculate the heat capacity  $C_M = T \partial S_M / \partial T$  from the entropy  $S_M = -k_B \sum_{i=-I}^I p_i \log p_i$ , which is a function of the thermodynamic state fully determined by  $B_{\text{hf}}(T)$  and  $T$ . In the fitting routine  $\mu_e(T)$  is found at an arbitrary temperature  $T$  by solving the equation  $\mu_e(T) - \mu_e^\infty - \chi_{\text{ion}}(\langle b_{\text{hf}}(T, \mu_e(T)) \rangle) = 0$  treating  $\mu_e^\infty$  as the fitting parameter.

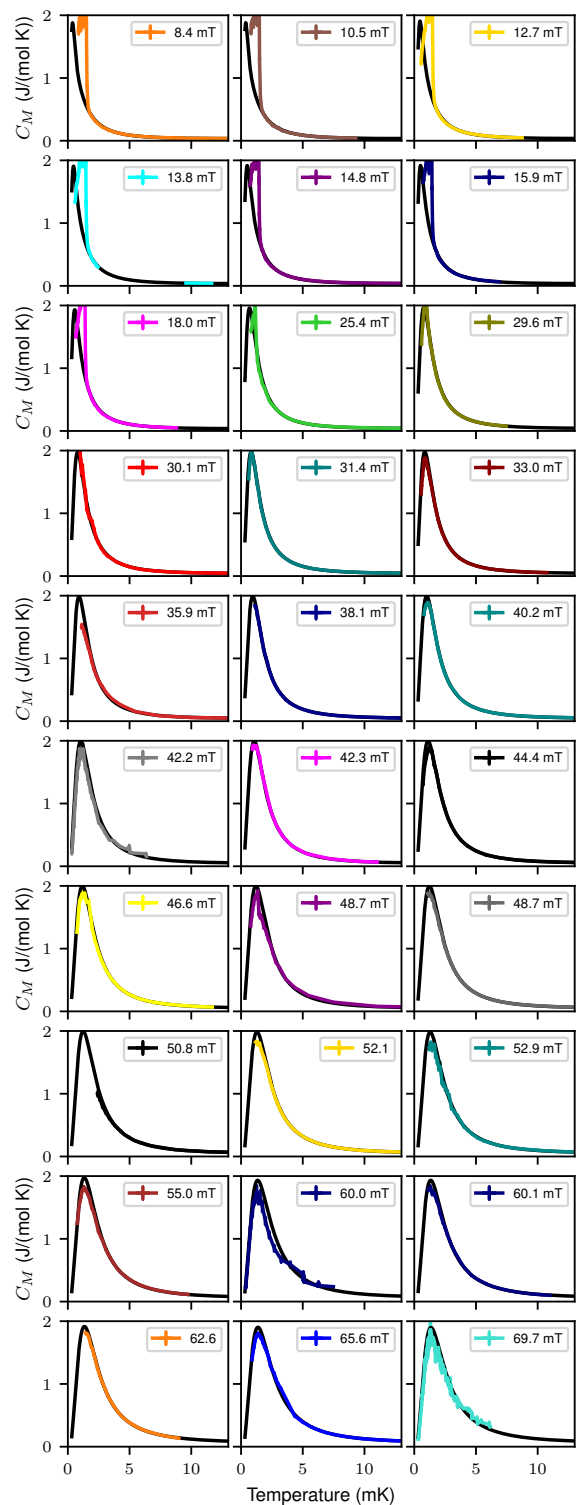


FIG. S1. Fitting hyperfine Schottky model to data at various external fields. The fits are shown by the black lines. The fitting interval is 1.7–13 mK. In fields up to 34 mT, we observe a discrepancy between the data and the model at low temperature associated with the AFM1/AFM2 transition. At higher fields the  $T < 1.7$  mK data systematically undercut the model. This small discrepancy of unknown origin demonstrates the increasing complexity of  $\text{YbRh}_2\text{Si}_2$  as  $T \rightarrow 0$ .

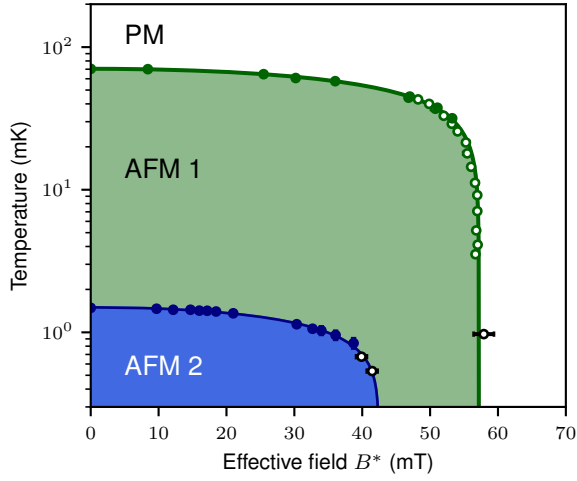


FIG. S2. The phase diagram of  $\text{YbRh}_2\text{Si}_2$  as a function of effective field  $B^*$  and temperature. In these coordinates both phase boundaries have conventional shape with no backturn. The significance of  $B^*$  inside the AFM2 dome remains an open question.

The value of  $\chi_{\text{ion}} = \partial\mu_e^\infty/B_{\text{ext}}$  is itself field dependent. Here, we obtain it, similar to Eq. (S10), from the 13 mK susceptibility data [33] as  $\chi_{\text{ion}}(B_{\text{ext}}) = 1.05\chi_m(B_{\text{ext}}, 13 \text{ mK})/\mu_0 N_A$ , leading to a good agreement between the two methods of determining  $\mu_e^\infty(B_{\text{ext}})$ , see Fig. 2. One may also derive  $\chi_{\text{ion}}$  from the heat capacity data simultaneously with the determination of  $\mu_e^\infty(B_{\text{ext}})$ , but this procedure is computationally complex and may suffer from noise in the determined  $\mu_e^\infty(B_{\text{ext}})$ .

Our fits take into account the heat capacity  $C = \gamma T$  of the heavy fermi liquid below 57 mT and  $C = a \log(T_0/T)T$  due to quantum-critical quasiparticles at higher fields. The field dependence of the Sommerfeld coefficient  $\gamma$ , constant  $a$ , and characteristic temperature  $T_0$  will be the subject of a future report.

### AFM1/PM PHASE BOUNDARY

We consider an ansatz

$$B_N^*(T) = \sqrt{a_3 T^3 + a_2 T^2 + a_1 T + a_0}, \quad (\text{S11})$$

for the effective critical field of AFM1. Taking  $\mu_e(B^*)$  from Eq. (S10) we derive the external critical field

$$B_N(T) = B_N^*(T) - \langle b_{\text{hf}}(T, \mu_e(B_N^*(T))) \rangle$$

and fit it to the experimental signatures of the AFM1/PM phase boundary, shown in Fig. 1. This procedure yields

$$\begin{array}{l|l} a_0 & 3.271 \cdot 10^3 \text{ mT}^2, \\ a_1 & 4.281 \cdot 10^{-1} \text{ mT}^2/\text{mK}, \\ a_2 & -3.110 \cdot 10^{-1} \text{ mT}^2/\text{mK}^2, \\ a_3 & -5.006 \cdot 10^{-3} \text{ mT}^2/\text{mK}^3. \end{array}$$

We note that this model involves no free parameters to describe the hyperfine field responsible for the backturn below 10 mK.

We also evaluate the effective field for the experimental signatures of this phase boundary, as shown in Fig. S2, and observe a conventional dome with no backturn. This supports the hypothesis that the antiferromagnetism in  $\text{YbRh}_2\text{Si}_2$  is driven by the effective field  $B^*$ .

### AFM1/AFM2 PHASE BOUNDARY

The phase boundary of AFM2 is described well by a similar ansatz,

$$B_A(T) = \sqrt{A_3 T^3 + A_2 T^2 + A_1 T + A_0}, \quad (\text{S12})$$

and the best fit parameters are

$$\begin{array}{l|l} A_0 & 1.096 \cdot 10^3 \text{ mT}^2, \\ A_1 & -1.112 \cdot 10^2 \text{ mT}^2/\text{mK}, \\ A_2 & 3.528 \cdot 10^2 \text{ mT}^2/\text{mK}^2, \\ A_3 & -5.120 \cdot 10^2 \text{ mT}^2/\text{mK}^3. \end{array}$$

Similar to  $B_N^*(T)$  the AFM1/AFM2 phase boundary can be considered in the temperature-effective field plane, see Fig. S2. For this phase boundary a conventional dome is observed, consistent with the AFM2 order being suppressed by the effective field  $B^*$ . Nevertheless, the dome has similar shape in  $B_A(T)$  and  $B_A^*(T)$  coordinates, as  $\langle b_{\text{hf}} \rangle$  is saturated along a significant part of this phase boundary.

### AFM1/AFM2 TRANSITION: HISTORY EFFECT

The complete sets of heat capacity peaks at AFM1/AFM2 and PM/AFM1 phase transitions are shown in Figs. S3 and S4 respectively. Although both transitions appear to be of second order at zero magnetic field [13, 14, 48], there is evidence for weak dependence of  $T_A$  signatures on the trajectory in  $(T, B_{\text{ext}})$  plane prior to crossing the phase boundary. This is evidenced by a double peak observed at 14.7 mT (Fig. S3) when the sample is “final field cooled”, i.e. cooled and subsequently measured at the same field (this is the natural approach in the experiment with aluminium heat switch above its switching field of 10 mT [14]). In contrast, when the sample is cooled in 80 mT with the field lowered after reaching the base temperature (with the lead heat switch with a higher switching field [14]), the double peak effectively disappears (Fig. S3, 14.8 mT) and the AFM2 order survives to a slightly higher temperature on warmup. This history effect may be linked to how the AFM2 magnetic domains respond to magnetic field. No history effects were observed below 11 mT; at higher fields “final field cooled” measurements are excluded from the phase diagram shown in Fig. 1.

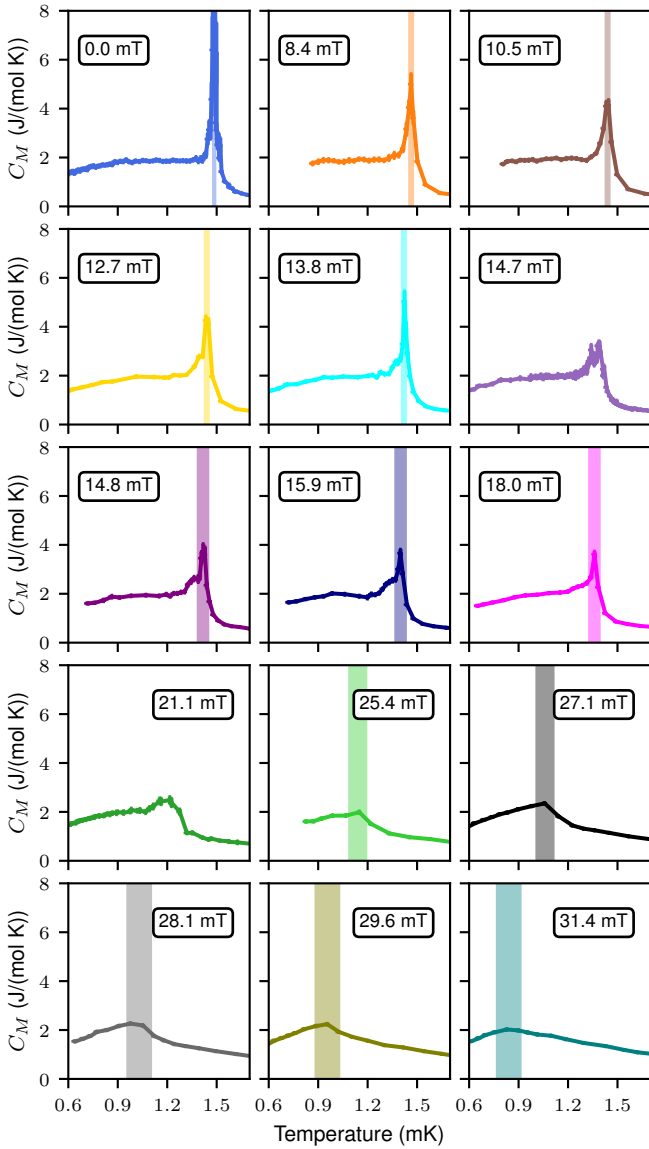


FIG. S3. Evolution of the  $T_A$  transition peak with external magnetic field. Estimated  $T$  position and uncertainty marked by the band. The “final field cooled” measurements above 11 mT (14.7 mT and 21.1 mT) are excluded from the phase diagram shown in Fig. 1.

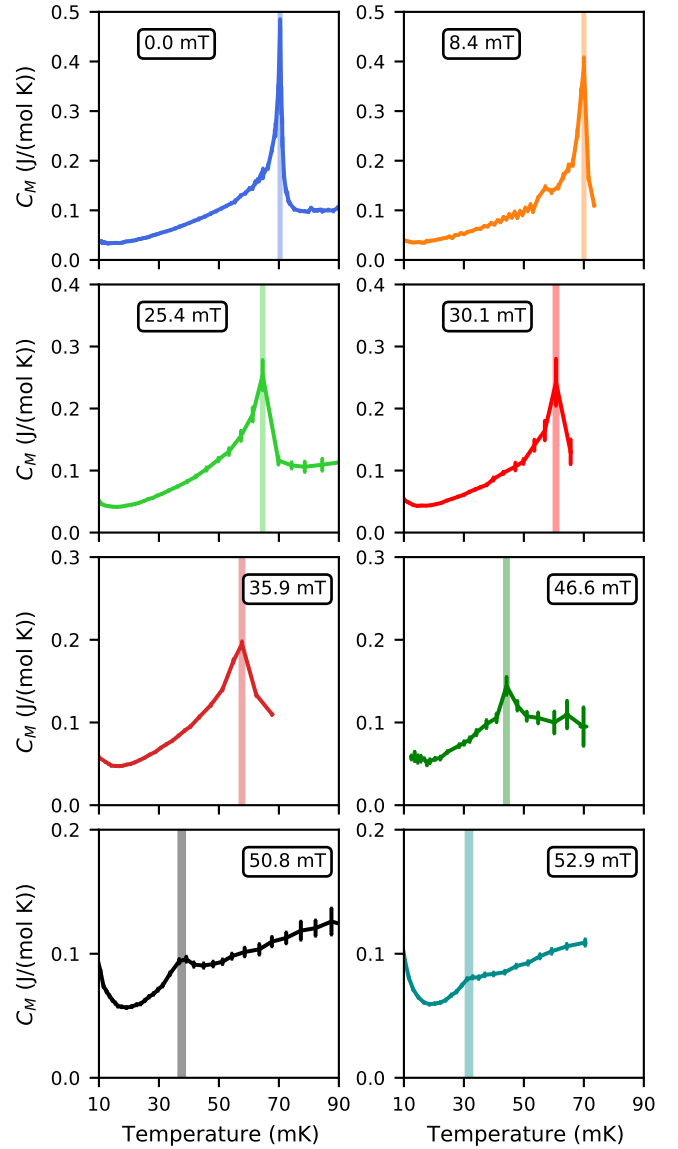


FIG. S4. Evolution of the  $T_N$  transition peak with external magnetic field. Estimated  $T$  position and uncertainty marked by the band.

\* jan.knapp@rhul.ac.uk, l.v.levitin@rhul.ac.uk, j.saunders@rhul.ac.uk

- [1] P. Gegenwart, J. Custers, C. Geibel, K. Neumaier, T. Tayama, K. Tenya, O. Trovarelli, and F. Steglich, Magnetic-field induced quantum critical point in  $\text{YbRh}_2\text{Si}_2$ , *Physical Review Letters* **89**, 056402 (2002).
- [2] J. Custers, P. Gegenwart, K. Neumaier, H. Wilhelm, N. Oeschler, K. Ishida, Y. Kitaoka, C. Geibel, and F. Steglich, Quantum criticality in  $\text{YbRh}_2\text{Si}_2$ , *Journal of Physics: Condensed Matter* **15**, S2047 (2003).

- [3] H. Pfau, S. Hartmann, U. Stockert, P. Sun, S. Lausberg, M. Brando, S. Friedemann, C. Krellner, C. Geibel, S. Wirth, S. Kirchner, E. Abrahams, Q. Si, and F. Steglich, Thermal and electrical transport across a magnetic quantum critical point, *Nature* **484**, 493 (2012).
- [4] P. Gegenwart, T. Westerkamp, C. Krellner, Y. Tokiwa, S. Paschen, C. Geibel, F. Steglich, E. Abrahams, and Q. Si, Multiple energy scales at a quantum critical point, *Science* **315**, 969 (2007).
- [5] P. Gegenwart, Q. Si, and F. Steglich, Quantum criticality in heavy-fermion metals, *Nature Physics* **4**, 186 (2008).
- [6] S. Friedemann, T. Westerkamp, M. Brando, N. Oeschler, S. Wirth, P. Gegenwart, C. Krellner, C. Geibel, and F. Steglich, Detaching the antiferromagnetic quantum

- critical point from the Fermi-surface reconstruction in  $\text{YbRh}_2\text{Si}_2$ , *Nature Physics* **5**, 465 (2009).
- [7] G. Knebel, R. Boursier, E. Hassinger, G. Lapertot, P. G. Niklowitz, A. Pourret, B. Salce, J. P. Sanchez, I. Sheikin, P. Bonville, H. Harima, and J. Flouquet, Localization of 4f state in  $\text{YbRh}_2\text{Si}_2$  under magnetic field and high pressure: Comparison with  $\text{CeRh}_2\text{Si}_2$ , *Journal of the Physical Society of Japan* **75**, 114709 (2006).
- [8] Z. F. Weng, M. Smidman, L. Jiao, X. Lu, and H. Q. Yuan, Multiple quantum phase transitions and superconductivity in ce-based heavy fermions, *Reports on Progress in Physics* **79**, 094503 (2016).
- [9] S. Nakatsuji, K. Kuga, Y. Machida, T. Tayama, T. Sakakibara, Y. Karaki, H. Ishimoto, S. Yonezawa, Y. Maeno, E. Pearson, G. G. Lonzarich, L. Balicas, H. Lee, and Z. Fisk, Superconductivity and quantum criticality in the heavy-fermion system  $\beta\text{-YbAlB}_4$ , *Nature Physics* **4**, 603 (2008).
- [10] E. Schuberth, M. Tippmann, L. Steinke, S. Lausberg, A. Steppke, M. Brando, C. Krellner, C. Geibel, R. Yu, Q. Si, and F. Steglich, Emergence of superconductivity in the canonical heavy-electron metal  $\text{YbRh}_2\text{Si}_2$ , *Science* **351**, 485 (2016).
- [11] D. Nguyen, A. Sidorenko, M. Taupin, G. Knebel, G. Lapertot, E. Schuberth, and S. Paschen, Superconductivity in an extreme strange metal, *Nature Communications* **12**, 10.1038/s41467-021-24670-z (2021).
- [12] L. V. Levitin, J. Knapp, P. Knappová, M. Lucas, J. Nyéki, P. Heikkinen, A. Casey, A. Ho, P. Coleman, C. Geibel, K. Kliemt, C. Krellner, M. Brando, and J. Saunders, Odd-parity superconductivity underpinned by antiferromagnetism in heavy fermion metal  $\text{YbRh}_2\text{Si}_2$  (2024), in preparation.
- [13] J. Knapp, L. Levitin, J. Nyéki, A. Ho, B. Cowan, J. Saunders, M. Brando, C. Geibel, K. Kliemt, and C. Krellner, Electronuclear transition into a spatially modulated magnetic state in  $\text{YbRh}_2\text{Si}_2$ , *Physical Review Letters* **130**, 126802 (2023).
- [14] J. Knapp, L. V. Levitin, J. Nyéki, M. Brando, and J. Saunders, Precise calorimetry of small metal samples using noise thermometry, *Journal of Low Temperature Physics* **217**, 638 (2024).
- [15] S. Friedemann, S. Wirth, N. Oeschler, C. Krellner, C. Geibel, F. Steglich, S. MaQuilon, Z. Fisk, S. Paschen, and G. Zwirgagl, Hall effect measurements and electronic structure calculations on  $\text{YbRh}_2\text{Si}_2$  and its reference compounds  $\text{LuRh}_2\text{Si}_2$  and  $\text{YbIr}_2\text{Si}_2$ , *Physical Review B* **82**, 035103 (2010).
- [16] K. Kummer, S. Patil, A. Chikina, M. Güttler, M. Höppner, A. Generalov, S. Danzenbächer, S. Seiro, A. Hannaske, C. Krellner, Y. Kucherenko, M. Shi, M. Radovic, E. Rienks, G. Zwirgagl, K. Matho, J. W. Allen, C. Laubschat, C. Geibel, and D. V. Vyalikh, Temperature-independent Fermi surface in the Kondo lattice  $\text{YbRh}_2\text{Si}_2$ , *Physical Review X* **5**, 011028 (2015).
- [17] G. Zwirgagl, The utility of band theory in strongly correlated electron systems, *Reports on Progress in Physics* **79**, 124501 (2016).
- [18] Y. Li, Q. Wang, Y. Xu, W. Xie, and Y. F. Yang, Nearly degenerate  $p_x + ip_y$  and  $d_{x^2-y^2}$  pairing symmetry in the heavy fermion superconductor  $\text{YbRh}_2\text{Si}_2$ , *Physical Review B* **100**, 085132 (2019).
- [19] M. Güttler, K. Kummer, K. Kliemt, C. Krellner, S. Seiro, C. Geibel, C. Laubschat, Y. Kubo, Y. Sakurai, D. V. Vyalikh, and A. Koizumi, Visualizing the Kondo lattice crossover in  $\text{YbRh}_2\text{Si}_2$  with Compton scattering, *Physical Review B* **103**, 115126 (2021).
- [20] K. Ishida, D. E. MacLaughlin, B. L. Young, K. Okamoto, Y. Kawasaki, Y. Kitaoka, G. J. Nieuwenhuys, R. H. Heffner, O. O. Bernal, W. Higemoto, A. Koda, R. Kadono, O. Trovarelli, C. Geibel, and F. Steglich, Low-temperature magnetic order and spin dynamics in  $\text{YbRh}_2\text{Si}_2$ , *Physical Review B* **68**, 184401 (2003).
- [21] S. Hamann, J. Zhang, D. Jang, A. Hannaske, L. Steinke, S. Lausberg, L. Pedrero, C. Klingner, M. Baenitz, F. Steglich, C. Krellner, C. Geibel, and M. Brando, Evolution from ferromagnetism to antiferromagnetism in  $\text{Yb}(\text{Rh}_{1-x}\text{Co}_x)\text{Si}_2$ , *Physical Review Letters* **122**, 077202 (2019).
- [22] Q. Si, S. Rabello, K. Ingersent, and J. L. Smith, Locally critical quantum phase transitions in strongly correlated metals, *Nature* **413**, 804 (2001).
- [23] P. Coleman and A. J. Schofield, Quantum criticality, *Nature* **433**, 226 (2005).
- [24] Q. Si and F. Steglich, Heavy Fermions and quantum phase transitions, *Science* **329**, 1161 (2010).
- [25] F. Steglich, Heavy fermions: superconductivity and its relationship to quantum criticality, *Philosophical Magazine* **94**, 3259 (2014).
- [26] M. H. Schubert, Y. Tokiwa, S. H. Hübner, M. Mchawalat, E. Blumenröther, H. S. Jeevan, and P. Gegenwart, Tuning low-energy scales in  $\text{YbRh}_2\text{Si}_2$  by non-isoelectronic substitution and pressure, *Physical Review Research* **1**, 032004(R) (2019).
- [27] S. Paschen and Q. Si, Quantum phases driven by strong correlations, *Nature Reviews Physics* **3**, 9 (2020).
- [28] E. Schuberth, S. Wirth, and F. Steglich, Nuclear-order-induced quantum criticality and Heavy-Fermion superconductivity at ultra-low temperatures in  $\text{YbRh}_2\text{Si}_2$ , *Frontiers in Electronic Materials* **2**, 10.3389/fe-mat.2022.869495 (2022).
- [29] E. Abrahams and P. Wölfle, Critical quasiparticle theory applied to heavy fermion metals near an antiferromagnetic quantum phase transition, *Proceedings of the National Academy of Sciences* **109**, 3238 (2012).
- [30] E. Abrahams, J. Schmalian, and P. Wölfle, Strong-coupling theory of heavy-fermion criticality, *Physical Review B* **90**, 045105 (2014).
- [31] P. Wölfle and E. Abrahams, Spin-flip scattering of critical quasiparticles and the phase diagram of  $\text{YbRh}_2\text{Si}_2$ , *Physical Review B* **92**, 155111 (2015).
- [32] S. Watanabe and K. Miyake, Quantum valence criticality as an origin of unconventional critical phenomena, *Physical Review Letters* **105**, 186403 (2010).
- [33] L. Steinke, E. Schuberth, S. Lausberg, M. Tippmann, A. Steppke, C. Krellner, C. Geibel, F. Steglich, and M. Brando, Ultra-low temperature ac susceptibility of the heavy-fermion superconductor  $\text{YbRh}_2\text{Si}_2$ , *Journal of Physics: Conference Series* **807**, 052007 (2017).
- [34] I. Nowik and S. Ofer, Mössbauer studies of  $^{170}\text{Yb}$  in several paramagnetic salts, *Journal of Physics and Chemistry of Solids* **29**, 2117 (1968).
- [35] J. Plessel, M. M. Abd-Elmeguid, J. P. Sanchez, G. Knebel, C. Geibel, O. Trovarelli, and F. Steglich, Unusual behavior of the low-moment magnetic ground state of  $\text{YbRh}_2\text{Si}_2$  under high pressure, *Physical Review B* **67**, 180403(R) (2003).

- [36] J. Flouquet and W. D. Brewer, Hyperfine interaction studies of local moments in metals, *Physica Scripta* **11**, 199 (1975).
- [37] J. Flouquet, Kondo coupling, hyperfine and exchange interactions, *Le Journal de Physique Colloques* **39**, C6 (1978).
- [38] P. Bonville, B. Canaud, J. Hammann, J. A. Hodges, P. Imbert, G. Jéhanno, A. Severing, and Z. Fisk, Magnetic ordering and hybridisation in  $\text{YbCu}_4$ , *Journal de Physique I* **2**, 459 (1992).
- [39] P. Bonville, J. A. Hodges, P. Imbert, G. Jéhanno, D. Jaccard, and J. Sierro, Magnetic ordering and paramagnetic relaxation of  $\text{Yb}^{3+}$  in  $\text{YbNi}_2\text{Si}_2$ , *Journal of Magnetism and Magnetic Materials* **97**, 178 (1991).
- [40] P. Bonville, P. Imbert, G. Jéhanno, F. Gonzalez–Jimenez, and F. Hartmann–Boutron, Emission Mössbauer spectroscopy and relaxation measurements in hyperfine levels out of thermal equilibrium: Very–low–temperature experiments on the Kondo alloy  $\text{Au}^{170}\text{Yb}$ , *Physical Review B* **30**, 3672 (1984).
- [41] J. Kondo, Internal magnetic field in rare earth metals, *Journal of the Physical Society of Japan* **16**, 1690 (1961).
- [42] The measured susceptibility leads to the enhancement of the magnetic induction  $B = (1 + \chi)B_{\text{ext}}$  inside  $\text{YbRh}_2\text{Si}_2$  over the external field  $B_{\text{ext}}$  by about 20%. This effect should be incorporated in future theoretical models of the magnetism in  $\text{YbRh}_2\text{Si}_2$ .
- [43] H. Eisenlohr and M. Vojta, Limits to magnetic quantum criticality from nuclear spins, *Physical Review B* **103**, 064405 (2021).
- [44] D. Bitko, T. F. Rosenbaum, and G. Aeppli, Quantum critical behavior for a model magnet, *Physical Review Letters* **77**, 940 (1996).
- [45] M. Libersky, R. D. McKenzie, D. M. Silevitch, P. C. E. Stamp, and T. F. Rosenbaum, Direct observation of collective electronuclear modes about a quantum critical point, *Physical Review Letters* **127**, 207202 (2021).
- [46] J. Banda, D. Hafner, J. F. Landaeta, E. Hassinger, K. Mitsumoto, M. Giovannini, J. G. Sereni, C. Geibel, and M. Brando, Electronuclear quantum criticality (2023), arXiv:2308.15294.
- [47] F. Bangma, L. Levitin, M. Lucas, A. Casey, J. Nyeki, I. Broeders, A. Sutton, B. Andraka, S. Julian, J. Saunders, and A. McCollam, Diverse influences of hyperfine interactions on strongly correlated electron states (2023), arXiv:2305.17088.
- [48] C. Krellner, S. Hartmann, A. Pikul, N. Oeschler, J. G. Donath, C. Geibel, F. Steglich, and J. Wosnitza, Violation of critical universality at the antiferromagnetic phase transition of  $\text{YbRh}_2\text{Si}_2$ , *Physical Review Letters* **102**, 196402 (2009).